

# Robust Geometry and Reflectance Disentanglement for 3D Face Reconstruction from Sparse-view Images

Daisheng Jin<sup>1</sup> Jiangbei Hu<sup>1,2</sup> Baixin Xu<sup>1</sup> Yuxin Dai<sup>1</sup> Chen Qian<sup>3</sup> Ying He<sup>1\*</sup>  
<sup>1</sup>Nanyang Technological University <sup>2</sup>Dalian University of Technology <sup>3</sup>SenseTime Research

## Abstract

This paper presents a novel two-stage approach for reconstructing human faces from sparse-view images, a task made challenging by the unique geometry and complex skin reflectance of each individual. Our method focuses on decomposing key facial attributes, including geometry, diffuse reflectance, and specular reflectance, from ambient light. Initially, we create a general facial template from a diverse collection of individual faces, capturing essential geometric and reflectance characteristics. Guided by this template, we refine each specific face model in the second stage, which further considers the interaction between geometry and reflectance, as well as the subsurface scattering effects on facial skin. Our method enables the reconstruction of high-quality facial representations from as few as three images, offering improved geometric accuracy and reflectance detail. Through comprehensive evaluations and comparisons, our method demonstrates superiority over existing techniques. Our method effectively disentangles geometry and reflectance components, leading to enhanced quality in synthesizing new views and opening up possibilities for applications such as relighting and reflectance editing. We will make the code publicly available.

## 1. Introduction

3D human face reconstruction finds widespread applications in various fields, including game design and film production. Developments in neural rendering techniques have shown promising performance and advantages in synthesizing photo-realistic images for complex scenes [2, 28, 29, 37]. Alongside these advancements, there has been a great deal of research on reconstructing head and facial attributes from images using implicit neural representations [15, 31, 32, 41, 53]. By addressing the shortcomings of traditional explicit methods [24, 33] based on the 3D Morphable Model (3DMM) [5], such as reliance on mesh resolution and challenges in handling topological

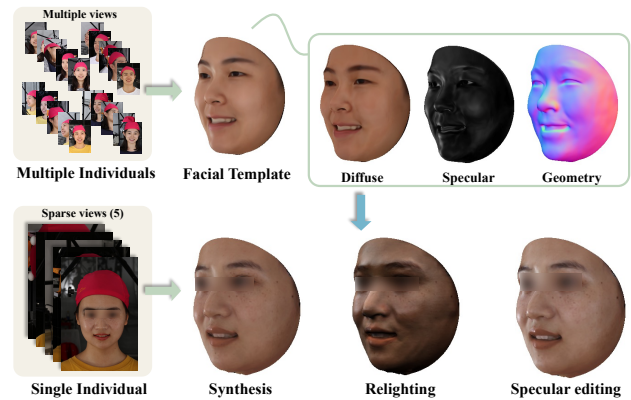


Figure 1. Our algorithm learns a general facial template from multi-view images of multiple individuals with distinct key facial attributes. This template enables photorealistic novel-view synthesis for each individual, as well as specular editing and relighting.

changes. These methods demonstrate their effectiveness in 3D face reconstruction from low-view images [41], expression transfer [1, 19, 26], and animations [16, 53, 54].

In 3D face model rendering, both accurate shape attributes and high-quality reflectance properties are essential for synthesizing photorealistic faces. Thus, robustly decomposing key facial attributes including geometry, diffuse and specular reflectance, and ambient light is a crucial task, which not only enhances the accuracy of face reconstruction but also opens up possibilities for more applications like relighting [6, 10, 11, 25, 49]. However, most previous studies only use neural networks to learn radiance and geometric information from pictures, without taking into account the effect of rendering-related physical information such as facial skin characteristics and ambient lighting conditions. NeRV [36], PhySG [47], and following methods [7, 8, 12, 18, 27, 30] incorporate the Bidirectional Reflectance Distribution Functions (BRDFs) into the neural rendering framework, which can decompose and jointly reconstruct the shape, reflectance, and illumination of the scene. Nonetheless, these methods primarily concentrate on non-biological materials like steel, stone, and plastic, which are not suitable for decomposing 3D face models

\*Corresponding author: Y. He (yhe@ntu.edu.sg).

that possess complex attributes. NeuFace [52] introduces an approximated BRDF integration and learns the physically meaningful underlying representations for 3D face reconstruction. Nevertheless, NeuFace often converges to a sub-optimal solution under sparse-view settings, in which specular reflectance is absent, and all radiance is derived from diffuse attributes. In addition, the accuracy of geometry reconstruction was severely downgraded along with views decreasing. Therefore, it still poses a significant challenge to decompose shape, reflectance, and ambient light attributes from sparse view images in 3D face model reconstruction.

In this study, we propose a two-stage face decomposition framework for 3D face reconstruction from sparse-view images. We illustrate the pipeline of our proposed algorithm in Fig. 3. Based on the observation that human faces share similar geometric features and reflectance properties, we first derive a general facial template from images of a set of varied individual faces in the first stage. In the second stage, we employ the learned facial template with both geometry and reflectance attributes to refine the decomposition of each individual face model. In both stages, we decompose the shape and material attributes using a geometry module and a reflectance module, respectively.

Specifically, the geometry module consists of a template network and a deformation network. In the first stage, we can get a template model with common geometry features based on the training of multi-view images from varied faces, which can be further transformed to a specific individual face model by deformation. For the reflectance module, we introduce the Bidirectional Reflectance Distribution Function (BRDF) based on the Physically Based Rendering (PBR) framework [35]. We use a BRDF template network to learn the common features of diffuse and specular attributes and a BRDF offset network to reconstruct identity-related reflectance details. In the second stage, based on the learned template with geometry and reflectance attributes, we refine the attribute details from sparse-view images of each individual face model. To this end, we incorporate a signed distance field (SDF) displacement network and a reflectance offset network on the learned templates to capture high-frequency information on geometry and reflectance, respectively. In addition, we incorporate a diffuse offset network to take into account the effect of subsurface scattering, thus providing a more realistic simulation of the facial skin material. We summarize the main contributions of this study as follows:

- We propose a novel decomposition framework for human facial representations to learn a template with various attributes, including geometric features, diffuse reflectance, and specular reflectance.
- Based on the learned template, our framework can robustly decompose the attributes for each individual face model under as few as three-view images, attaining supe-

rior geometric accuracy and reflectance detail.

- The face decomposition results obtained through our framework can facilitate more realistic synthesis in novel views, as well as applications such as specular editing and relighting.

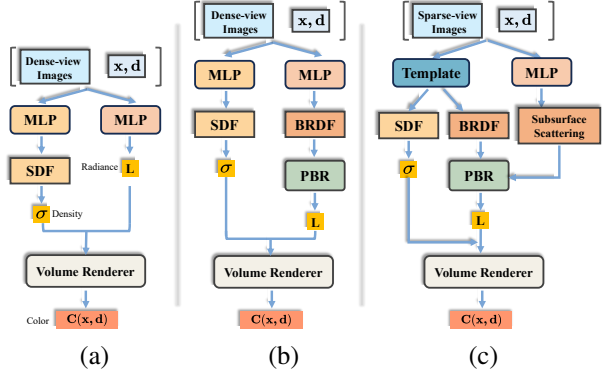


Figure 2. Overview. Framework (a) like VolSDF [45] accomplishes 3D reconstruction from dense images but does not decompose radiance-related factors. Framework (b) like PhySG introduces physically based rendering (PBR) to simulate real-world lighting. (c) We propose a novel geometry and reflectance decomposition framework for 3D face reconstruction from sparse views.

## 2. Related Work

### 2.1. Geometry Decomposition from Neural Fields

By training from multi-view images, NeRF [28] demonstrates its power in rendering high-quality images of novel views [2, 29, 39]. NeRF’s success lies in its implicit 3D representation, providing a conceptual understanding of 3D space. However, implicit 3D representations pose challenges in interpretability, as well as in editing and manipulation. Hence, the decomposition of geometry from the neural field, transforming it into explicit 3D representations like 3D meshes, becomes crucial. Nonetheless, due to the lack of consideration of geometry decomposition, simply extracting 3D mesh from the density of NeRF can not achieve a satisfactory geometry decomposition result. To deal with this, VolSDF [45] and NeuS [40] incorporate the Signed Distance Field (SDF) to facilitate a smoother 3D representation in the volume rendering pipeline. The SDF allows for better decoupling of geometry information from multi-view images, enabling the reconstruction of finely detailed 3D meshes.

### 2.2. Physically Based Rendering

To achieve a more photorealistic rendering effect, physically based rendering (PBR) [35] is proposed to simulate the light and surfaces using real-world optical principles. Reversely, physically based inverse rendering seeks

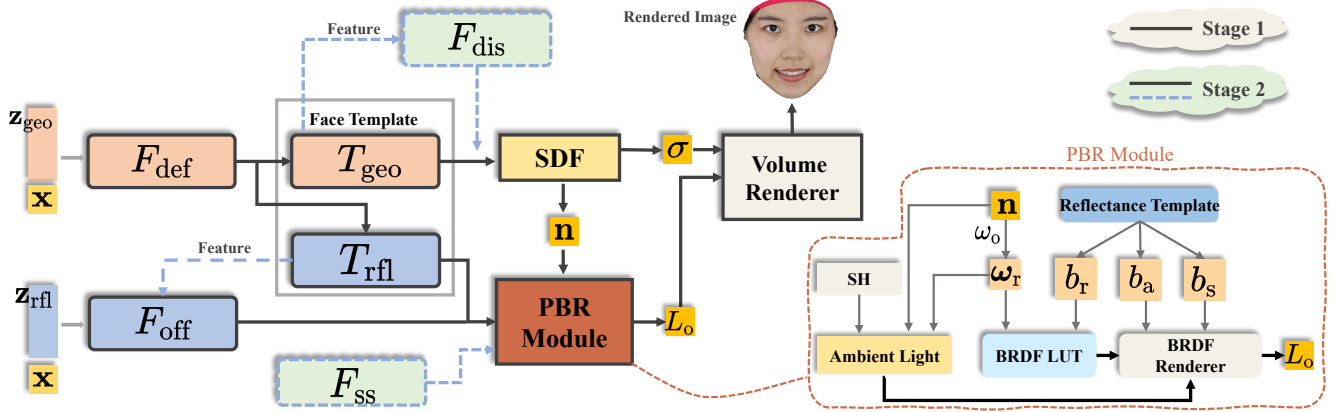


Figure 3. Pipeline. We propose a geometry and reflectance decomposition framework for 3D face reconstruction from multi-view images. We first learn a general facial template from multi-view images of multiple individuals in Stage 1. Then the learned facial template guides the further attribute refinement for each individual face model in Stage 2.

a way to decompose light and surface factors from the images [3, 4, 7, 30]. IDR [44] proposes a surface reconstruction method that simultaneously disentangles the geometry and appearance. Subsequent works incorporate inverse rendering into the neural rendering pipeline. For light representation, PhySG [47] utilizes Spherical Gaussian (SG), and Neural-PIL [8] employs an illumination embedding to represent ambient light in inverse rendering. For objects with special material, Nero [27] devises a method for high-reflectance objects, while subsurface scattering is considered in [9] for translucent objects. NeuFace [52] proposes a decomposition pipeline for human faces, taking into account the sophisticated properties of facial skin reflectance. However, face decomposition is an ill-posed problem, and there is no ground truth for reflectance components, leading NeuFace to frequently fail in accurately decomposing specular reflectance. Additionally, NeuFace does not consider the effect of subsurface scattering on facial skin, resulting in less realistic PBR [43]. In this work, with our novel face template and the single-person refinement module, which further considers subsurface scattering effects, we can robustly decompose geometry and reflectance in a more realistic manner from sparse-view images.

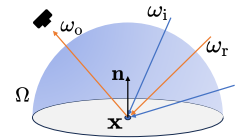
### 2.3. Facial Template

Given the inherent similarities among human faces, it is intuitive to develop a template that serves as a prior to enhance facial reconstruction. Based on a large amount of facial data, 3DMM [5] builds a statistical model to describe the transformation of shape and expression, which is widely used in face recognition [50], 3D reconstruction, face editing [14, 31], etc. As implicit neural representation shows extraordinary efficacy for 3D representation, numerous studies [41, 46, 51, 53] construct 3D parametric face or head models based on neural networks, yielding improved

geometric details for faces or heads. Besides, Han *et al.* [17] build a 3D morphable face with reflectance on BFM09 [34] for material editing. Our Stage 1 model incorporates prior knowledge of both facial geometry and reflectance, which enables a robust decomposition during single-person refinement under sparse views.

### 3. Preliminary

The effectiveness of PBR has been validated by numerous studies [21, 39, 52] for photo realistic rendering in scenarios with complex reflection properties. Inspired by these work, we formulate the output radiance  $L_o \in \mathbb{R}^3$  at surface position  $\mathbf{x} \in \mathbb{R}^3$  along output direction  $\omega_o \in \mathbb{R}^3$  as:  $L_o(\mathbf{x}, \omega_o) = \int_{\Omega} f(\mathbf{x}, \omega_i, \omega_o) L_i(\mathbf{x}, \omega_i) (\omega_i \cdot \mathbf{n}) d\omega_i$ , where  $f$  represents the BRDF evaluation,  $L_i \in \mathbb{R}^3$  is the incident light intensity from input direction  $\omega_i \in \mathbb{R}^3$ ,  $\mathbf{n} \in \mathbb{R}^3$  is the surface normal. To decouple the view-dependent and view-independent radiance, we decompose  $L_o$  into the diffuse term and the specular term by:



$$L_o(\mathbf{x}, \omega_o) = \underbrace{\frac{b_a(\mathbf{x})}{\pi} \int_{\Omega} L_i(\mathbf{x}, \omega_i) (\omega_i \cdot \mathbf{n}) d\omega_i}_{\text{diffuse}} + \underbrace{\int_{\Omega} f_s(\mathbf{x}, \omega_i, \omega_o; b_s(\mathbf{x}), b_r(\mathbf{x})) L_i(\mathbf{x}, \omega_i) (\omega_i \cdot \mathbf{n}) d\omega_i}_{\text{specular}},$$

where  $b_a(\mathbf{x}) \in \mathbb{R}^3$ ,  $b_s(\mathbf{x}) \in \mathbb{R}^4$ ,  $b_r(\mathbf{x}) \in \mathbb{R}$  are diffuse albedo, specular, and roughness fields obtained from BRDF, respectively.  $f_s$  represents the BRDF evaluation that only accounts for the specular property. Furthermore, we improve the efficiency of integration computation by using the

approximated pre-computed method [8] as:

$$L_o(\mathbf{x}, \boldsymbol{\omega}_o) \approx \underbrace{\frac{b_a(\mathbf{x})}{\pi} \hat{L}_i(\mathbf{n}, 1)}_{\text{diffuse}} + \underbrace{\hat{f}_s(\mathbf{x}; b_s(\mathbf{x}), b_r(\mathbf{x})) \hat{L}_i(\boldsymbol{\omega}_r, b_r(\mathbf{x}))}_{\text{specular}}, \quad (1)$$

where  $\boldsymbol{\omega}_r \in \mathbb{R}^3$  represent the mirrored view direction,  $\hat{L}_i$  is the integration of input light,  $\hat{f}_s$  is the integration of specular reflectance. Specifically, we employ a small MLP to simulate two look-up-textures (LUT)  $B_0$  and  $B_1$  [22] to calculate the BRDF integration term:

$$\hat{f}_s(\mathbf{x}) = b_s(\mathbf{x})[F_0(\boldsymbol{\omega}_o, \mathbf{n})B_0(\boldsymbol{\omega}_o \cdot \mathbf{n}, b_r(\mathbf{x})) + B_1(\boldsymbol{\omega}_o \cdot \mathbf{n}, b_r(\mathbf{x}))], \quad (2)$$

where  $F_0$  is the Fresnel term at normal incidence as [8]. For light representation, we use spherical harmonics [38] to approximate ambient light by:

$$L_i(\boldsymbol{\omega}_i) \approx \sum_{\ell=0}^k \sum_{m=-\ell}^{\ell} c_{\ell}^m Y_{\ell}^m(\boldsymbol{\omega}_i), \quad (3)$$

where  $Y$  represents spherical basis functions and  $c$  denotes corresponding coefficients. Considering that the facial material is not of high specular reflectance, we set the order as  $k = 10$  [11]. To integrate incident light rays, the light for the specular term can be integrated to the mirrored direction of the observation view, denoted as  $\hat{L}_i(\boldsymbol{\omega}_r, b_r)$ , and light for the diffuse term (Lambertian) can be approximated by  $\hat{L}_i(\mathbf{n}, 1)$  [8], which assumes light in the normal direction hits a completely rough surface. For our SH light representation, we integrate the two terms as [52].

**Volume rendering.** Following most volume rendering work [28], we calculate the color by integrating the radiance  $L_o$  and density  $\sigma \in \mathbb{R}$  along the ray  $\mathbf{r}$  as:

$$\mathbf{C}(\mathbf{r}) = \int_{t'}^{t''} L_o(\mathbf{x}(t), \boldsymbol{\omega}_o) \sigma(t) T(t) dt, \quad (4)$$

where  $\mathbf{x}(t)$  represents the coordinates of a point in the ray, with  $t'$  and  $t''$  as the starting and ending points along the ray, respectively.  $T(t) = \exp(-\int_{t'}^t \sigma(t) dt)$ , which can be considered as the radiance attenuation rate caused by hitting particles along the ray.

## 4. Method

Typical human faces share common features, such as two eyes and one nose, with variations in characteristics such as shape, skin color, and skin texture. To better utilize the shared features of human faces, we divide the decomposition process into two stages to learn the neural fields of human faces from multi-view images. As shown in Fig. 3, we first create a general facial template with geometry and reflectance attributes from a collection of portraits of multiple individuals in stage 1 (Sect. 4.1). Subsequently, in stage

2, we refine the specific attributes for each individual face model based on the learned facial template under sparse-view settings (Sect. 4.2).

### 4.1. Generating Facial Template

Given a collection of portraits of multiple individuals  $\{\mathcal{I}_i\}$ , we first learn a general facial template with both geometry and reflectance attributes.

**Geometry template.** Following the previous work [41, 51], we jointly employ a template network  $T_{\text{geo}}$  and a deformation network  $F_{\text{dfm}}$  to reconstruct the geometry (represented by signed distance field  $\mathcal{S}$ ) from given images. As illustrated in Fig. 3, we formulate the geometry network as:

$$\mathcal{S}(\mathbf{x}) = T_{\text{geo}}(F_{\text{dfm}}(\mathbf{x}, \mathbf{z}_{\text{geo}})), \quad (5)$$

where  $\mathbf{x} \in \mathbb{R}^3$  is a query spatial point,  $\mathcal{S}(\mathbf{x}) \in \mathbb{R}$  returns the signed distance value. We take  $\mathbf{z}_{\text{geo}} \in \mathbb{R}^{128}$  as an identity-related latent code that encodes geometry, so we can get the unique SDF for each individual. Similar to VolSDF [45], we convert the SDF value to density  $\sigma$  and then feed it into the volume rendering block.

**Reflectance template.** Apart from geometry attributes, we take into account reflectance attributes that are equally crucial, including diffuse and specular factors. Human faces tend to respond similarly to ambient light due to the shared underlying biological and structural properties, indicating the viability of creating a reflectance template as a prior for individual reconstruction under sparse-view images. In stage 1, our goal is to build a smooth template that implies the underlying common representation of human faces, rather than a detailed reconstruction. Therefore, we disregard the subsurface scattering effects in stage 1 and consider them in stage 2 for individual reconstruction.

To obtain the reflectance attributes, we approximate the Bidirectional Reflectance Distribution Function (BRDF) by the network that consists of a reflectance template  $T_{\text{rfl}}$  and a BRDF offset network  $F_{\text{ofs}}$ . Similar to the geometry template, we leverage  $T_{\text{rfl}}$  to fit the general facial BRDF for multiple individuals and then offset the BRDF value of the query points on each face model through  $F_{\text{ofs}}$ . We formulate the calculation of BRDF  $\mathcal{B}(\mathbf{x})$  as follows:

$$\mathcal{B}(\mathbf{x}) = T_{\text{rfl}}[F_{\text{dfm}}(\mathbf{x}, \mathbf{z}_{\text{geo}})] + w F_{\text{ofs}}(\mathbf{x}, \mathbf{z}_{\text{rfl}}), \quad (6)$$

where the query points  $\mathbf{x}$  in the observation space are deformed to the surface of the facial template through  $F_{\text{dfm}}$ , and  $T_{\text{rfl}}$  return the corresponding BRDF attributes  $\mathcal{B}(\mathbf{x}) = [b_a(\mathbf{x}), b_s(\mathbf{x}), b_r(\mathbf{x})] \in \mathbb{R}^8$ . Then we learn the offset amount of BRDF through  $F_{\text{ofs}}$  to obtain the specific reflectance attributes for each individual. We introduce a reflectance latent code  $\mathbf{z}_{\text{rfl}} \in \mathbb{R}^{128}$  related to identity to distinguish the different reflectance features possessed by different people. In addition, we adjust the offset using a weight parameter  $w$ .

We apply a low weight,  $w = 0.05$ , as we prefer to have the template network primarily learn the reflectance properties rather than relying heavily on the BRDF offset network. To simulate ambient light, we apply the spherical harmonics as in Eq. (3) and integrate the lights as in [52].

After obtaining the geometry, reflectance, and ambient light information, we calculate the final color as Eq. (1-4). As shown in Fig. 1, a general facial template can be obtained and robustly decomposed into geometry, diffuse, and specular attributes.

## 4.2. Individual Decomposition under Sparse Views

Taking the facial template learned from Stage 1 as prior, we then perform a fine-detailed face decomposition from sparse-view images of a single individual in Stage 2.

**Geometry displacement.** The geometric template  $T_{\text{geo}}$  represents only a rough shape with shared features of multiple human faces. The deformation net  $F_{\text{dfm}}$  transforms the points on the surface of the facial template to the surface of a specific individual’s face. However, the transformation is constrained, making it challenging to create topological features beyond the template domain and capture high-frequency details. Consequently, we incorporate a displacement network  $F_{\text{dis}}$  in stage 2 to modify the SDF obtained from the geometry template for a more accurate reconstruction. The offset term is integrated into Eq. (5):

$$\mathcal{S}(\mathbf{x}) = T_{\text{geo}}(F_{\text{dfm}}(\mathbf{x}, \mathbf{z}_{\text{geo}})) + F_{\text{dis}}(\mathbf{x}). \quad (7)$$

**BRDF offset.** Based on the reflectance template  $T_{\text{rfl}}$  learned from stage 1, we calculate the offset value of BRDF through  $F_{\text{ofs}}$ , similar to stage 1, to obtain the specific BRDF attributes for each individual. To address the distinct diversity between diffuse albedo  $b_a$ , specular  $b_s$  and roughness  $b_r$ , we add a learnable weight term  $\mathbf{W}(\mathbf{x}) = [\mathbf{w}_a, \mathbf{w}_s, \mathbf{w}_r]$  to control the contribution of each BRDF attribute from the reflectance template  $T_{\text{rfl}}$ , where  $\mathbf{w}_a \in \mathbb{R}^3$ ,  $\mathbf{w}_s \in \mathbb{R}^4$ ,  $\mathbf{w}_r \in \mathbb{R}$  are the weights for diffuse albedo, specular, and roughness, respectively. Thus, we obtain the BRDF attributes as:

$$\mathcal{B}(\mathbf{x}) = \mathbf{W}(\mathbf{x}) \cdot T_{\text{rfl}}[F_{\text{dfm}}(\mathbf{x}, \mathbf{z}_{\text{geo}})] + F_{\text{ofs}}(\mathbf{x}). \quad (8)$$

Considering that the diffuse albedo attribute has a large variation between different people, we initialize  $\mathbf{w}_a$  with relatively low values.

**Attribute synergy.** In our framework, we decompose facial attributes into two components, *i.e.*, geometry and reflectance, but they are not isolated and can enhance each other corporately. In certain situations, there can be confusion between geometry and reflectance, which may result in inaccuracies during the decomposition and reconstruction process. For instance, a dark region in an image can be caused by sunken or dark spots on the face. Conventional neural rendering techniques rely solely on color information

from images, making it hard to distinguish such ambiguous scenes, often leading to incorrect reconstruction. Since our method can decouple rough geometry and reflectance attributes in stage 1, we utilize the prior from the reflectance template to facilitate geometry inference, and vice versa. Specifically, we obtain the displacement  $\mathcal{D}(\mathbf{x})$  as follows:

$$\mathcal{D}(\mathbf{x}) = F_{\text{dis}}(\mathbf{x}, \text{concat}(\mathbf{f}_{\text{def}}, \mathbf{f}_{\text{geo}}, \mathbf{f}_{\text{rfl}})), \quad (9)$$

where  $\mathbf{f}_{\text{dfm}} \in \mathbb{R}^{128}$ ,  $\mathbf{f}_{\text{geo}} \in \mathbb{R}^{128}$ , and  $\mathbf{f}_{\text{rfl}} \in \mathbb{R}^{128}$  are extracted feature vectors from the output of the final hidden layer of  $F_{\text{dfm}}$ ,  $T_{\text{geo}}$ , and  $T_{\text{rfl}}$ , respectively. We also extract another feature vector  $\mathbf{f}_{\text{dis}} \in \mathbb{R}^{64}$  from  $F_{\text{dis}}$  to provide more geometry information to the BRDF offset network  $F_{\text{ofs}}$ . Similarly, we calculate the BRDF offset  $\mathcal{B}_{\text{ofs}}(\mathbf{x})$  as:

$$\mathcal{B}_{\text{ofs}}(\mathbf{x}) = F_{\text{ofs}}(\mathbf{x}, \text{concat}(\mathbf{f}_{\text{def}}, \mathbf{f}_{\text{geo}}, \mathbf{f}_{\text{dis}}, \mathbf{f}_{\text{rfl}})). \quad (10)$$

Our ablation study experiments validate the effectiveness of this attribute synergy module in the accuracy of both geometry reconstruction and rendering results.

### Subsurface scattering offset.

Human facial skin is much more complex than non-biological materials such as metal and plastic. Previous work [13] demonstrates that realistic face rendering should take into account subsurface scattering effects, which can be for-

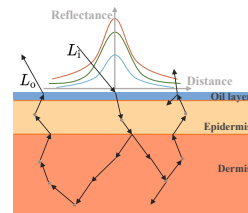


Figure 4. Subsurface scattering effects on skin

ulated in a three-layer model (as shown in Fig. 4). For specular terms, light can be assumed to reflect off the surface at the incident points. For diffuse terms, a ray of light can penetrate the skin’s surface, pass through the three layers, reflect multiple times in the subsurface, and then return to the surface. As a result, the output light shifts a small distance on the surface from the point of incidence. This process is known as subsurface scattering, which can be formulated as  $L_o(\mathbf{x}_o, \omega_o) = \int_A \int_{\Omega} S(\mathbf{x}_o, \omega_o, \mathbf{x}_i, \omega_i) L_i(\mathbf{x}_i, \omega_i) (\omega_i \cdot \mathbf{n}) d\omega_i dA$ , where  $\mathbf{x}_i$  and  $\mathbf{x}_o$  are the positions of the light incident and output points, respectively,  $A$  is a small area around  $\mathbf{x}_o$ , and  $S$  is the scattering evaluation.

BRDF is limited to considering light rays that scatter back from their point of incidence. Simulating surface scattering directly, however, incurs a substantial computational cost. To enhance the quality of face reconstruction, we incorporate subsurface scattering as an offset  $F_{\text{ss}}$  to the BRDF’s diffuse term. To streamline the process, we assume uniformity in the subsurface scattering properties within a sufficiently small region. By employing scattering profiles [23], we can approximate the subsurface scattering reflectance in this region. As illustrated in Fig. 4, the

scattering profiles depict the correlation between the shift length (the distance between the incident and output points) and the reflectance associated with subsurface scattering. As previous work [23] suggests, one can approximate each RGB channel of the scattering profiles using a combination of six Gaussian functions. We employ the weights of these Gaussian functions to form a feature vector  $\mathbf{f}_{\text{sp}}^{\mathbf{x}} \in \mathbb{R}^{18}$ , which represents the scattering profile of the point  $\mathbf{x}$ . Consequently, we calculate the offset of the diffuse term as:

$$F_{\text{ss}}(\mathbf{x}) = v\hat{F}_{\text{sp}}(\mathbf{x}, \mathbf{f}_{\text{sp}}^{\mathbf{x}})\hat{L}_i(\mathbf{x}, \mathcal{E}(\mathbf{x})), \quad (11)$$

where  $v$  is the weight of scatter offset,  $\hat{F}_{\text{sp}}$  is a network to integrate scattering reflectance,  $\hat{L}_i$  is a network to integrate the incoming light in a small region around  $\mathbf{x}$ , and  $\mathcal{E}(\mathbf{x}) \in \mathbb{R}^3$  is a learnable vector that defines the size of the integration domain. The values of  $\mathbf{f}_{\text{sp}}^{\mathbf{x}}$  and  $\mathcal{E}(\mathbf{x})$  are obtained through an MLP. We refer readers to the supplementary for more details of the network architecture.

### 4.3. Training Losses

For both stages, we consider reconstruction losses including the pixel-wise color loss  $\mathcal{L}_{\text{col}} = \|\mathbf{C} - \mathbf{C}_{\text{gt}}\|_1$  and the eikonal loss  $\mathcal{L}_{\text{eik}} = (\|\nabla \mathcal{S}\|_2 - 1)^2$ . Similar to NeuFace [52], we incorporate a regularization term  $\mathcal{L}_{\text{light}}$  to assume a nearly white ambient light and penalize the specular energy by  $\mathcal{L}_{\text{spec}}$ . Besides, we add  $\mathcal{L}_{\text{code}} = \|\mathbf{z}_{\text{geo}}\|_2 + \|\mathbf{z}_{\text{rfi}}\|_2$  to regularize the latent codes. To avoid a large variation between the predict reflectance attributes and the template during training, we apply a constraint to BRDF offset as  $\mathcal{L}_{\text{ofs}} = \|\mathcal{B}_{\text{ofs}}(\mathbf{x})\|_1$ . As a result, we formulate the loss function in stage 1 as follows:

$$\mathcal{L}_{\text{st1}} = \mathcal{L}_{\text{col}} + \mathcal{L}_{\text{eik}} + \mathcal{L}_{\text{light}} + \mathcal{L}_{\text{spec}} + \mathcal{L}_{\text{ofs}} + \mathcal{L}_{\text{code}}. \quad (12)$$

For the second stage, we add additional displacement loss  $\mathcal{L}_{\text{dis}}$  and scatter offset loss  $\mathcal{L}_{\text{ss}}$ :

$$\mathcal{L}_{\text{st2}} = \mathcal{L}_{\text{st1}} + \mathcal{L}_{\text{dis}} + \mathcal{L}_{\text{ss}}, \quad (13)$$

where  $\mathcal{L}_{\text{dis}} = \|\mathcal{D}(\mathbf{x})\|_1$  and  $\mathcal{L}_{\text{ss}} = \|F_{\text{ss}}(\mathbf{x})\|_1$  are regularization losses aimed at constraining high values of the displacement and the subsurface scattering offset.

## 5. Experimental Results

### 5.1. Setup

**Dataset and metrics.** We evaluate our method on a large human face dataset *Facescape* [42]<sup>1</sup>. We utilize authorized data from approximately 30 individuals, with 4 of them being from the publishable list. To protect the privacy of other

<sup>1</sup>To comply with the dataset’s privacy policy, we have masked the eye regions of individuals whose identities are not authorized for disclosure.

identities that are not in the publishable list, we employ mosaic technology in the eyes region. We assess the quality of image rendering using the PSNR, SSIM, and LPIPS [48] metrics, and the Chamfer distance (CD) for evaluating the accuracy of geometry reconstruction. We compared our method with two 3D reconstruction methods VolSDF [45], DeformHead [41] and three BRDF decomposition methods PhySG [47], TensoIR [20], and NeuFace [52].

**Implementation details.** We use 10 subjects with 10 views each for the training of the facial template. In terms of refinement for individual face models, we utilize 3, 5, and 10 views of subjects that were not involved in the template training process. The 10-view experiments mainly test our performance under a low-view setting. We employ the Adam optimizer with an initial learning rate  $1 \times 10^{-4}$  to train both stages for 3000 epochs. Additionally, we add a calibration module as [52] to mitigate the exposure differences between various views and apply this calibration to all the methods for a fair comparison. For more implementation details, please refer to the supplementary material.

### 5.2. Evaluation & Comparison

To corroborate the effectiveness of our proposed decomposition framework in the reconstruction of appearance and geometry, we conducted a comprehensive comparison with state-of-the-art methods. These methods are categorized into two groups: geometry-oriented methods, which include VolSDF [45] and DeformHead [41]; and decomposition-based methods, including PhySG [47], TensoIR [20], NeuFace [52], and our own method. As shown in Tab. 1, we enumerate the quantitative performance of different methods in the evaluation metrics. To assess the performance capability under sparse-view images, we conducted tests on 20 subjects with 3, 5, and 10 views, respectively. The visual results of the reconstruction from 3 views are presented in Fig. 5, showcasing the synthesized rendering images from a novel viewpoint, the geometric reconstruction, and the decomposition of diffuse and specular attributes.

**Decomposition-based methods.** Our method exhibits superior performance in novel view rendering and geometry reconstruction compared to other reflectance decomposition methods. In contrast to PhySG and TensoIR, designed for common objects, our method significantly outperforms them across all metrics. This is due to the complexity of facial material reflectance, which requires specialized reflectance modeling. Our general facial template learned from stage 1 plays a crucial role in facilitating robust decomposition and reconstruction in stage 2, particularly when handling sparse views. NeuFace, which is customized for facial skin, poses a challenge due to its non-robust decomposition of geometry and reflectance attributes. As shown in Fig. 6, it often happens in NeuFace that all reflectance is induced from albedo, but the specular

	3 views				5 views				10 views			
	PSNR↑	SSIM↑	LPIPS↓	CD↓	PSNR↑	SSIM↑	LPIPS↓	CD↓	PSNR↑	SSIM↑	LPIPS↓	CD↓
VolSDF [45]	22.95	0.868	6.92	18.28	25.45	0.897	6.09	7.40	27.34	0.910	5.18	5.25
DeformHead [41]	<b>26.02</b>	0.886	5.76	9.60	26.41	0.879	4.83	8.44	27.35	0.891	5.20	5.42
PhySG [47]	22.03	0.863	7.81	70.87	22.69	0.872	7.05	63.20	23.11	0.876	7.12	55.7
TensoIR [20]	22.35	0.645	7.14	28.60	24.61	0.704	5.86	17.10	26.14	0.769	4.73	10.10
NeuFace [52]	23.54	0.876	5.78	15.74	25.81	0.904	4.75	8.62	27.19	0.914	4.03	6.40
Ours	25.54	<b>0.902</b>	<b>4.46</b>	<b>9.27</b>	<b>26.73</b>	<b>0.911</b>	<b>3.83</b>	<b>7.00</b>	<b>27.64</b>	<b>0.920</b>	<b>3.86</b>	5.53

Table 1. Evaluation. The LPIPS and CD metrics are measured on scales of  $10^{-2}$  and  $10^{-3}$ , respectively. The best and second-best results are highlighted in red and orange, respectively.

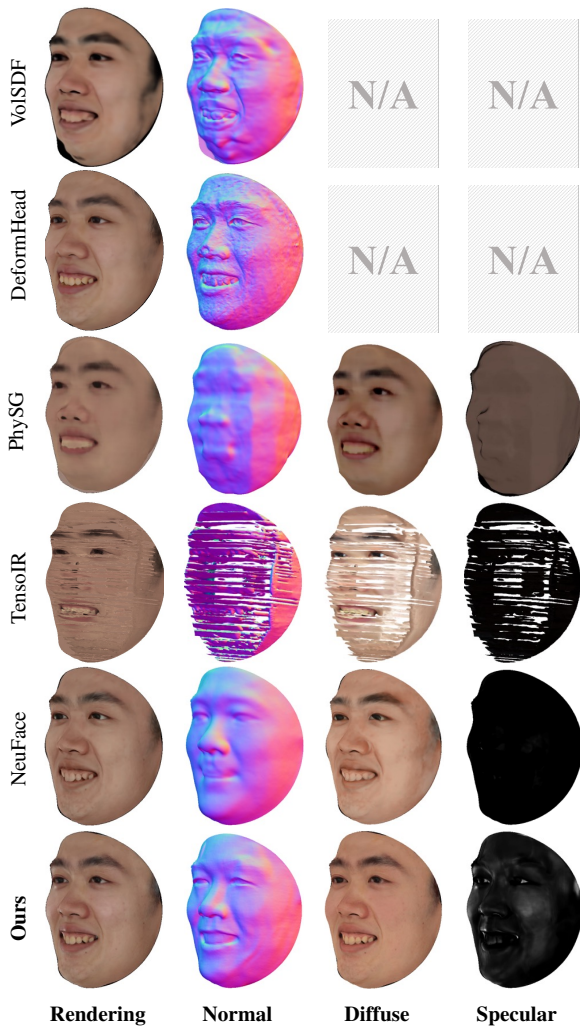


Figure 5. Visualization of 3-view reconstruction results. VolSDF and DeformHead do not incorporate reflectance attributes, resulting in the absence of corresponding outcomes. Our method outperforms others in terms of decomposition accuracy, geometric reconstruction quality, and novel view synthesis.

term is entirely absent. This degenerate Lambertian model may reduce the realism of the synthesized rendering output, especially for elements such as teeth, eyes, or the oily layer on facial skin, which often exhibit specular reflection

effects. In contrast, we are able to stably decompose the diffuse and specular properties, resulting in more realistic rendering effects. Considering that there is no ground truth for specular reflectance, we introduce a straightforward metric called specular failure rate, representing the percentage of entirely empty specular output. This metric facilitates a quantitative comparison between our method and NeuFace. According to the statistics, our method achieves a specular failure rate of 0, whereas NeuFace’s specular failure rates are 30%, 25%, and 20% under 3 views, 5 views, and 10 views, respectively. Additionally, we demonstrate higher accuracy in geometric reconstruction, whereas the quality of NeuFace’s geometry deteriorates significantly as the number of views decreases.

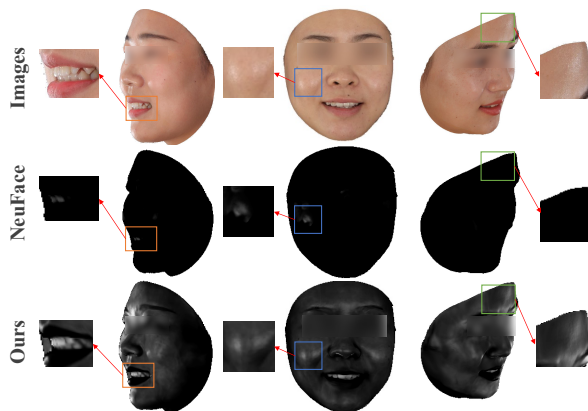


Figure 6. Comparison with NeuFace [52] in terms of specular reflectance decomposition.

**Geometry-oriented methods.** Our method demonstrates a comparable level of accuracy in geometry reconstruction compared to VolSDF and DeformHead. VolSDF exhibits poor 3D reconstruction results in sparse view settings. While DeformHead achieves a more robust and detailed 3D reconstruction utilizing a geometry template, it is overly sensitive to geometry deformation. Although the PSNR of our method is a bit lower than that of DeformHead under 3 views, our LPIPS outperforms it, indicating more photorealistic synthesis results. Instances of failure in ren-

dering and reconstruction have been observed with VoISDF and DeformHead, with failure rates of 21.7% and 6.7%, respectively. We exclude these failures from the comparison.

### 5.3. Ablation Studies

We select a subset of 10 subjects from the dataset to test the effectiveness of the subsurface scattering offset  $F_{ss}$  and the attribute synergy module. From Tab. 2, we observe that the attribute synergy module appears to contribute to geometry decomposition, and its absence leads to a noticeable decrease in geometric accuracy. In addition, the subsurface scatter offset module can enhance the realism of the synthesized images from novel views, which is suggested by improvements in the LPIPS metric. As shown in Fig. 7, the subsurface scattering offset introduces additional details in light reflection on the skin, resulting in more photorealistic rendering results. Regarding the attribute synergy module, the exchange of information between geometry and reflectance enables a more accurate decomposition, as is evident in the details of geometry reconstruction.

	PSNR $\uparrow$	SSIM $\uparrow$	LPIPS $\downarrow$	CD $\downarrow$
w/o attribute synergy	24.79	0.876	4.90	8.80
w/o scattering offset	24.60	0.874	5.73	8.61
Ours	<b>25.65</b>	<b>0.882</b>	<b>4.45</b>	<b>7.94</b>

Table 2. Comparative evaluation metrics for ablation studies.

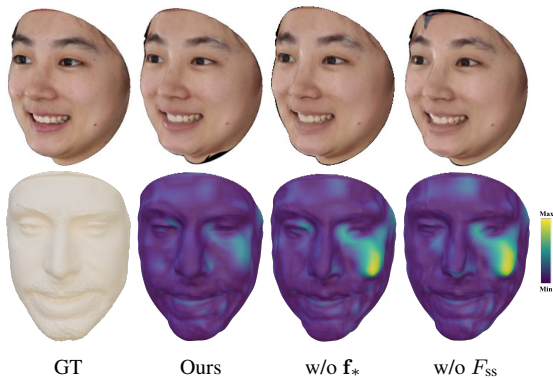


Figure 7. Ablation. Comparison of rendered images (top row) and reconstructed geometries (bottom row) under full modules, without attribute synergy module  $f_*$ , without subsurface scattering  $F_{ss}$ , respectively.

### 5.4. Applications

**Specular editing.** Our advanced decomposition of diffuse and specular reflectances allows us to easily adjust the specular reflectance, resulting in the ability to make faces appear shinier or dimmer. We display the specular editing results in Fig. 8. Specifically, we increase the specular weight by 1.5 times, while maintaining the overall specular distribution unchanged. As a result, the edited images can retain their photorealistic appearance.

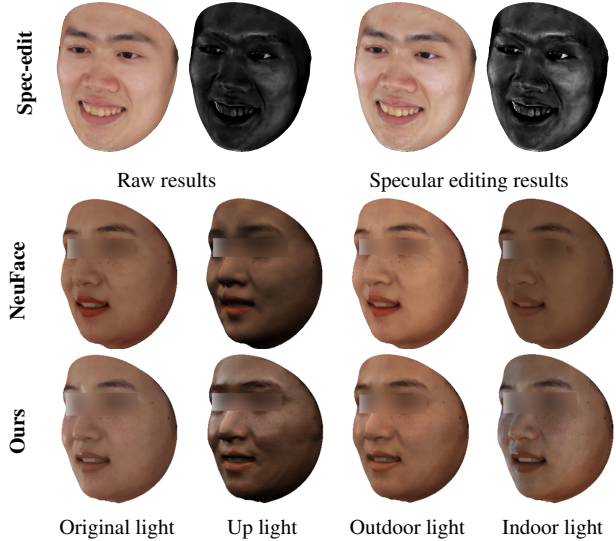


Figure 8. Applications. Specular editing (top row) and relighting (middle and bottom rows).

**Relighting.** Decomposing reflectance and ambient light facilitate the relighting of human faces without altering their inherent properties. As shown in Fig. 5, we conducted a comparison of the relighting effects between our method and NeuFace in sparse view settings. Our method excels in decomposing specular reflectance, leading to more vibrant and realistic relighting outcomes under varying ambient lighting conditions [11].

## 6. Conclusion

We propose a novel face decomposition method capable of rendering and reconstructing 3D human faces from sparse-view images. Our framework first learns a facial template with both decomposed geometry and reflectance attributes from multi-view images of different individuals. Then we utilize the prior knowledge of the facial template and further consider the interaction between geometry and reflectance, as well as subsurface scattering effects, which enable our method to achieve robust face decomposition from sparse-view images. Based on decomposed facial attributes, our method achieves superior results in the rendering and geometric reconstruction of 3D human faces and can be utilized for relighting and specular editing.

**Limitations & Future work.** As we focus on face decomposition, it is hard to extend to general objects directly with our method. Additionally, capturing intricate geometry details, such as teeth, proves challenging due to the complexity of decomposition and the inherent ill-posed nature of the problem. Moreover, we could involve techniques such as hash encoding [29] to accelerate our method and leverage fine-detailed 3D prior or reflectance ground truth for a better decomposition effect in further research work.

## References

- [1] ShahRukh Athar, Zexiang Xu, Kalyan Sunkavalli, Eli Shechtman, and Zhixin Shu. Rignerf: Fully controllable neural 3d portraits. In *Proceedings of the IEEE/CVF conference on Computer Vision and Pattern Recognition*, pages 20364–20373, 2022. 1
- [2] Jonathan T Barron, Ben Mildenhall, Matthew Tancik, Peter Hedman, Ricardo Martin-Brualla, and Pratul P Srinivasan. Mip-nerf: A multiscale representation for anti-aliasing neural radiance fields. In *Proceedings of the IEEE/CVF International Conference on Computer Vision*, pages 5855–5864, 2021. 1, 2
- [3] Sai Bi, Zexiang Xu, Pratul Srinivasan, Ben Mildenhall, Kalyan Sunkavalli, Miloš Hašan, Yannick Hold-Geoffroy, David Kriegman, and Ravi Ramamoorthi. Neural reflectance fields for appearance acquisition. *arXiv preprint arXiv:2008.03824*, 2020. 3
- [4] Sai Bi, Zexiang Xu, Kalyan Sunkavalli, David Kriegman, and Ravi Ramamoorthi. Deep 3d capture: Geometry and reflectance from sparse multi-view images. In *Proceedings of the IEEE/CVF conference on computer vision and pattern recognition*, pages 5960–5969, 2020. 3
- [5] Volker Blanz and Thomas Vetter. A morphable model for the synthesis of 3d faces. In *Seminal Graphics Papers: Pushing the Boundaries, Volume 2*, pages 157–164. 2023. 1, 3
- [6] Mark Boss, Varun Jampani, Kihwan Kim, Hendrik Lensch, and Jan Kautz. Two-shot spatially-varying brdf and shape estimation. In *Proceedings of the IEEE/CVF Conference on Computer Vision and Pattern Recognition*, pages 3982–3991, 2020. 1
- [7] Mark Boss, Raphael Braun, Varun Jampani, Jonathan T Barron, Ce Liu, and Hendrik Lensch. Nerf: Neural reflectance decomposition from image collections. In *Proceedings of the IEEE/CVF International Conference on Computer Vision*, pages 12684–12694, 2021. 1, 3
- [8] Mark Boss, Varun Jampani, Raphael Braun, Ce Liu, Jonathan Barron, and Hendrik Lensch. Neural-pil: Neural pre-integrated lighting for reflectance decomposition. *Advances in Neural Information Processing Systems*, 34: 10691–10704, 2021. 1, 3, 4
- [9] Chengqian Che, Fujun Luan, Shuang Zhao, Kavita Bala, and Ioannis Gkioulekas. Towards learning-based inverse sub-surface scattering. In *2020 IEEE International Conference on Computational Photography (ICCP)*, pages 1–12. IEEE, 2020. 3
- [10] Zhaoxi Chen and Ziwei Liu. Relighting4d: Neural relightable human from videos. In *European Conference on Computer Vision*, pages 606–623. Springer, 2022. 1
- [11] Zhang Chen, Anpei Chen, Guli Zhang, Chengyuan Wang, Yu Ji, Kiriakos N Kutulakos, and Jingyi Yu. A neural rendering framework for free-viewpoint relighting. In *Proceedings of the IEEE/CVF Conference on Computer Vision and Pattern Recognition*, pages 5599–5610, 2020. 1, 4, 8
- [12] Ziang Cheng, Hongdong Li, Yuta Asano, Yinqiang Zheng, and Imari Sato. Multi-view 3d reconstruction of a textureless smooth surface of unknown generic reflectance. In *Proceedings of the IEEE/CVF Conference on Computer Vision and Pattern Recognition*, pages 16226–16235, 2021. 1
- [13] Craig Donner and Henrik Wann Jensen. Light diffusion in multi-layered translucent materials. *ACM Transactions on Graphics (ToG)*, 24(3):1032–1039, 2005. 5
- [14] Yao Feng, Haiwen Feng, Michael J Black, and Timo Bolkart. Learning an animatable detailed 3d face model from in-the-wild images. *ACM Transactions on Graphics (ToG)*, 40(4): 1–13, 2021. 3
- [15] Guy Gafni, Justus Thies, Michael Zollhofer, and Matthias Nießner. Dynamic neural radiance fields for monocular 4d facial avatar reconstruction. In *Proceedings of the IEEE/CVF Conference on Computer Vision and Pattern Recognition*, pages 8649–8658, 2021. 1
- [16] Simon Giebenhain, Tobias Kirschstein, Markos Georgopoulos, Martin Rünz, Lourdes Agapito, and Matthias Nießner. Learning neural parametric head models. In *Proceedings of the IEEE/CVF Conference on Computer Vision and Pattern Recognition*, pages 21003–21012, 2023. 1
- [17] Yuxuan Han, Zhibo Wang, and Feng Xu. Learning a 3d morphable face reflectance model from low-cost data. In *Proceedings of the IEEE/CVF Conference on Computer Vision and Pattern Recognition*, pages 8598–8608, 2023. 3
- [18] Jon Hasselgren, Nikolai Hofmann, and Jacob Munkberg. Shape, light, and material decomposition from images using monte carlo rendering and denoising. *Advances in Neural Information Processing Systems*, 35:22856–22869, 2022. 1
- [19] Yang Hong, Bo Peng, Haiyao Xiao, Ligang Liu, and Juyong Zhang. Headnerf: A real-time nerf-based parametric head model. In *Proceedings of the IEEE/CVF Conference on Computer Vision and Pattern Recognition*, pages 20374–20384, 2022. 1
- [20] Haian Jin, Isabella Liu, Peijia Xu, Xiaoshuai Zhang, Songfang Han, Sai Bi, Xiaowei Zhou, Zexiang Xu, and Hao Su. Tensor: Tensorial inverse rendering. In *Proceedings of the IEEE/CVF Conference on Computer Vision and Pattern Recognition*, pages 165–174, 2023. 6, 7
- [21] James T Kajiya. The rendering equation. In *Proceedings of the 13th annual conference on Computer graphics and interactive techniques*, pages 143–150, 1986. 3
- [22] Brian Karis and Epic Games. Real shading in unreal engine 4. *Proc. Physically Based Shading Theory Practice*, 4(3):1, 2013. 4
- [23] Andrew Lauritzen. Gpu gems 3, 2007. 5, 6
- [24] Tianye Li, Timo Bolkart, Michael J Black, Hao Li, and Javier Romero. Learning a model of facial shape and expression from 4d scans. *ACM Trans. Graph.*, 36(6):194–1, 2017. 1
- [25] Zhengqin Li, Mohammad Shafiei, Ravi Ramamoorthi, Kalyan Sunkavalli, and Manmohan Chandraker. Inverse rendering for complex indoor scenes: Shape, spatially-varying lighting and svbrdf from a single image. In *Proceedings of the IEEE/CVF Conference on Computer Vision and Pattern Recognition*, pages 2475–2484, 2020. 1
- [26] Connor Lin, Koki Nagano, Jan Kautz, Eric Chan, Umar Iqbal, Leonidas Guibas, Gordon Wetzstein, and Sameh Khamis. Single-shot implicit morphable faces with consistent texture parameterization. In *ACM SIGGRAPH 2023 Conference Proceedings*, pages 1–12, 2023. 1

- [27] Yuan Liu, Peng Wang, Cheng Lin, Xiaoxiao Long, Jiepeng Wang, Lingjie Liu, Taku Komura, and Wenping Wang. Nero: Neural geometry and BRDF reconstruction of reflective objects from multiview images. *ACM Trans. Graph.*, 42(4):114:1–114:22, 2023. 1, 3
- [28] Ben Mildenhall, Pratul P Srinivasan, Matthew Tancik, Jonathan T Barron, Ravi Ramamoorthi, and Ren Ng. Nerf: Representing scenes as neural radiance fields for view synthesis. *Communications of the ACM*, 65(1):99–106, 2021. 1, 2, 4
- [29] Thomas Müller, Alex Evans, Christoph Schied, and Alexander Keller. Instant neural graphics primitives with a multiresolution hash encoding. *ACM Transactions on Graphics (ToG)*, 41(4):1–15, 2022. 1, 2, 8
- [30] Jacob Munkberg, Jon Hasselgren, Tianchang Shen, Jun Gao, Wenzheng Chen, Alex Evans, Thomas Müller, and Sanja Fidler. Extracting triangular 3d models, materials, and lighting from images. In *Proceedings of the IEEE/CVF Conference on Computer Vision and Pattern Recognition*, pages 8280–8290, 2022. 1, 3
- [31] Keunhong Park, Utkarsh Sinha, Jonathan T Barron, Sofien Bouaziz, Dan B Goldman, Steven M Seitz, and Ricardo Martin-Brualla. Nerfies: Deformable neural radiance fields. In *Proceedings of the IEEE/CVF International Conference on Computer Vision*, pages 5865–5874, 2021. 1, 3
- [32] Keunhong Park, Utkarsh Sinha, Peter Hedman, Jonathan T Barron, Sofien Bouaziz, Dan B Goldman, Ricardo Martin-Brualla, and Steven M Seitz. Hypernerf: a higher-dimensional representation for topologically varying neural radiance fields. *ACM Transactions on Graphics (TOG)*, 40(6):1–12, 2021. 1
- [33] Georgios Pavlakos, Vasileios Choutas, Nima Ghorbani, Timo Bolkart, Ahmed AA Osman, Dimitrios Tzionas, and Michael J Black. Expressive body capture: 3d hands, face, and body from a single image. In *Proceedings of the IEEE/CVF conference on computer vision and pattern recognition*, pages 10975–10985, 2019. 1
- [34] Pascal Paysan, Reinhard Knothe, Brian Amberg, Sami Romdhani, and Thomas Vetter. A 3d face model for pose and illumination invariant face recognition. In *2009 sixth IEEE international conference on advanced video and signal based surveillance*, pages 296–301. Ieee, 2009. 3
- [35] Matt Pharr, Wenzel Jakob, and Greg Humphreys. *Physically based rendering: From theory to implementation*. MIT Press, 2023. 2
- [36] Pratul P Srinivasan, Boyang Deng, Xiuming Zhang, Matthew Tancik, Ben Mildenhall, and Jonathan T Barron. Nerv: Neural reflectance and visibility fields for relighting and view synthesis. In *Proceedings of the IEEE/CVF Conference on Computer Vision and Pattern Recognition*, pages 7495–7504, 2021. 1
- [37] Matthew Tancik, Ethan Weber, Evonne Ng, Ruilong Li, Brent Yi, Terrance Wang, Alexander Kristoffersen, Jake Austin, Kamyar Salahi, Abhik Ahuja, et al. Nerfstudio: A modular framework for neural radiance field development. In *ACM SIGGRAPH 2023 Conference Proceedings*, pages 1–12, 2023. 1
- [38] Borom Tunwattanapong, Graham Fyffe, Paul Graham, Jay Busch, Xueming Yu, Abhijeet Ghosh, and Paul Debevec. Acquiring reflectance and shape from continuous spherical harmonic illumination. *ACM Transactions on graphics (TOG)*, 32(4):1–12, 2013. 4
- [39] Dor Verbin, Peter Hedman, Ben Mildenhall, Todd Zickler, Jonathan T Barron, and Pratul P Srinivasan. Ref-nerf: Structured view-dependent appearance for neural radiance fields. In *2022 IEEE/CVF Conference on Computer Vision and Pattern Recognition (CVPR)*, pages 5481–5490. IEEE, 2022. 2, 3
- [40] Peng Wang, Lingjie Liu, Yuan Liu, Christian Theobalt, Taku Komura, and Wenping Wang. Neus: Learning neural implicit surfaces by volume rendering for multi-view reconstruction. *Advances in Neural Information Processing Systems*, 34:27171–27183, 2021. 2
- [41] Baixin Xu, Jiarui Zhang, Kwan-Yee Lin, Chen Qian, and Ying He. Deformable model-driven neural rendering for high-fidelity 3d reconstruction of human heads under low-view settings. pages 17924–17934, 2023. 1, 3, 4, 6, 7
- [42] Haotian Yang, Hao Zhu, Yanru Wang, Mingkai Huang, Qiu Shen, Ruigang Yang, and Xun Cao. Facescape: a large-scale high quality 3d face dataset and detailed riggable 3d face prediction. In *Proceedings of the IEEE/cvf conference on computer vision and pattern recognition*, pages 601–610, 2020. 6
- [43] Jing Yang, Hanyuan Xiao, Wenbin Teng, Yunxuan Cai, and Yajie Zhao. Light sampling field and BRDF representation for physically-based neural rendering. In *The Eleventh International Conference on Learning Representations, ICLR 2023, Kigali, Rwanda, May 1-5, 2023*. OpenReview.net, 2023. 3
- [44] Lior Yariv, Yoni Kasten, Dror Moran, Meirav Galun, Matan Atzmon, Basri Ronen, and Yaron Lipman. Multiview neural surface reconstruction by disentangling geometry and appearance. *Advances in Neural Information Processing Systems*, 33:2492–2502, 2020. 3
- [45] Lior Yariv, Jiatao Gu, Yoni Kasten, and Yaron Lipman. Volume rendering of neural implicit surfaces. *Advances in Neural Information Processing Systems*, 34:4805–4815, 2021. 2, 4, 6, 7
- [46] Tarun Yenamandra, Ayush Tewari, Florian Bernard, Hans-Peter Seidel, Mohamed Elgharib, Daniel Cremers, and Christian Theobalt. i3dmm: Deep implicit 3d morphable model of human heads. In *Proceedings of the IEEE/CVF Conference on Computer Vision and Pattern Recognition*, pages 12803–12813, 2021. 3
- [47] Kai Zhang, Fujun Luan, Qianqian Wang, Kavita Bala, and Noah Snavely. Physg: Inverse rendering with spherical gaussians for physics-based material editing and relighting. In *Proceedings of the IEEE/CVF Conference on Computer Vision and Pattern Recognition*, pages 5453–5462, 2021. 1, 3, 6, 7
- [48] Richard Zhang, Phillip Isola, Alexei A Efros, Eli Shechtman, and Oliver Wang. The unreasonable effectiveness of deep features as a perceptual metric. In *Proceedings of the IEEE conference on computer vision and pattern recognition*, pages 586–595, 2018. 6

- [49] Xiuming Zhang, Pratul P Srinivasan, Boyang Deng, Paul Debevec, William T Freeman, and Jonathan T Barron. Nerfactor: Neural factorization of shape and reflectance under an unknown illumination. *ACM Transactions on Graphics (ToG)*, 40(6):1–18, 2021. [1](#)
- [50] Wenyi Zhao, Rama Chellappa, P Jonathon Phillips, and Azriel Rosenfeld. Face recognition: A literature survey. *ACM computing surveys (CSUR)*, 35(4):399–458, 2003. [3](#)
- [51] Mingwu Zheng, Hongyu Yang, Di Huang, and Liming Chen. Imface: A nonlinear 3d morphable face model with implicit neural representations. In *Proceedings of the IEEE/CVF Conference on Computer Vision and Pattern Recognition*, pages 20343–20352, 2022. [3](#), [4](#)
- [52] Mingwu Zheng, Haiyu Zhang, Hongyu Yang, and Di Huang. Neuface: Realistic 3d neural face rendering from multi-view images. In *Proceedings of the IEEE/CVF Conference on Computer Vision and Pattern Recognition*, pages 16868–16877, 2023. [2](#), [3](#), [4](#), [5](#), [6](#), [7](#)
- [53] Yufeng Zheng, Victoria Fernández Abrevaya, Marcel C Bühler, Xu Chen, Michael J Black, and Otmar Hilliges. Im avatar: Implicit morphable head avatars from videos. In *Proceedings of the IEEE/CVF Conference on Computer Vision and Pattern Recognition*, pages 13545–13555, 2022. [1](#), [3](#)
- [54] Zerong Zheng, Han Huang, Tao Yu, Hongwen Zhang, Yandong Guo, and Yebin Liu. Structured local radiance fields for human avatar modeling. In *Proceedings of the IEEE/CVF Conference on Computer Vision and Pattern Recognition*, pages 15893–15903, 2022. [1](#)